

Structures and distributions of SARS-CoV-2 spike proteins on intact virions

<https://doi.org/10.1038/s41586-020-2665-2>

Received: 2 July 2020

Accepted: 10 August 2020

Published online: 17 August 2020

 Check for updates

Zunlong Ke^{1,7}, Joaquin Oton^{1,7}, Kun Qu^{1,7}, Mirko Cortese², Vojtech Zila³, Lesley McKeane⁴, Takanori Nakane¹, Jasenko Zivanov¹, Christopher J. Neufeldt², Berati Cerikan², John M. Lu¹, Julia Peukes¹, Xiaoli Xiong¹, Hans-Georg Kräusslich^{3,5}, Sjors H. W. Scheres¹, Ralf Bartenschlager^{2,5,6} & John A. G. Briggs¹✉

Severe acute respiratory syndrome coronavirus 2 (SARS-CoV-2) virions are surrounded by a lipid bilayer from which spike (S) protein trimers protrude¹. Heavily glycosylated S trimers bind to the angiotensin-converting enzyme 2 receptor and mediate entry of virions into target cells^{2–6}. S exhibits extensive conformational flexibility: it modulates exposure of its receptor-binding site and subsequently undergoes complete structural rearrangement to drive fusion of viral and cellular membranes^{2,7,8}. The structures and conformations of soluble, overexpressed, purified S proteins have been studied in detail using cryo-electron microscopy^{2,7,9–12}, but the structure and distribution of S on the virion surface remain unknown. Here we applied cryo-electron microscopy and tomography to image intact SARS-CoV-2 virions and determine the high-resolution structure, conformational flexibility and distribution of S trimers in situ on the virion surface. These results reveal the conformations of S on the virion, and provide a basis from which to understand interactions between S and neutralizing antibodies during infection or vaccination.

The *Betacoronavirus* SARS-CoV-2^{13,14} is an enveloped virus containing a large nucleoprotein (N)-encapsidated positive-sense RNA genome¹⁵. Three transmembrane proteins are incorporated into the viral lipid envelope: S and two smaller proteins, membrane protein (M) and envelope protein (E)^{1,15}. When imaged by cryo-electron microscopy (cryo-EM), betacoronaviruses appear as approximately spherical particles with variable diameters centred around 100 nm, containing a dense viroplasm and bounded by a lipid bilayer from which prominent S trimers protrude^{16,17}. S trimers of SARS-CoV-2 bind to its receptor on the surface of target cells—angiotensin-converting enzyme 2 (ACE2)—and mediate subsequent viral uptake and fusion^{2–5,7}. In so doing, S undergoes a substantial structural rearrangement from the prefusion form to the postfusion form⁸. The overall architectures of both prefusion and postfusion forms are highly conserved among coronaviruses^{8,18,19}.

During infection, coronaviruses extensively remodel the internal membrane organization of the cell, generating viral replication organelles in which replication takes place^{20–22}. The S, M and E proteins are inserted into membranes of the endoplasmic reticulum and traffic to the endoplasmic reticulum–Golgi intermediate compartment (ERGIC). The encapsidated genome buds into the ERGIC to form virions, which are then trafficked to the plasma membrane and released^{20–22}. S is primed for membrane fusion by proteolytic cleavage at the S1–S2 site, and subsequently the S2' site²³.

The prefusion structures of S proteins from coronaviruses, including SARS-CoV-2 S, have been extensively studied using ectopic expression of soluble, secreted forms of S, followed by purification and cryo-EM^{2,7,9–11}. In the prefusion form, the receptor-binding domain (RBD)

sits at the top of a broad, trimeric spike above the fusion core. Three copies of the RBD are surrounded by three copies of the N-terminal domain (NTD) which display some mobility^{2,7–9}. In the closed prefusion conformation, all three copies of the RBD lie flat on the spike surface, largely occluding the receptor-binding site, whereas in the open prefusion conformation, one or multiple RBDs lift to expose the receptor-binding site^{2,7,9,10}. The surface of the trimer is extensively glycosylated with 22 potential N-linked glycosylation sites per monomer^{2,6,7}. After receptor binding, structural transition of the prefusion form to the postfusion form brings the fusion peptide and the transmembrane domain together at one end of a long, needle-like structure centred around a three-helix bundle⁸. Five N-linked glycans are spaced along the length of the postfusion spike⁸.

Fully understanding how S proteins function and how they interact with the immune system requires knowledge of the structures, conformations and distributions of S trimers within virions. In this study, we apply cryo-EM methods to study the structure, conformations and distributions of S trimers in situ on the virion surface.

To avoid artefacts associated with virus concentration or purification, we aimed to image SARS-CoV-2 virions from the supernatant of infected cells without further concentrating or purifying the virus. Vero E6 cells were infected with SARS-CoV-2 (isolate Germany/BavPat1/2020)²⁴. At 48 h after infection, the supernatant was clarified, inactivated by fixation with formaldehyde and stored at –80 °C. Western blot analysis revealed that approximately 45% of the total S protein monomers on virions had been cleaved at the multibasic cleavage site, resulting in S1 and S2 peptides (Fig. 1a). The fixed supernatant

¹Structural Studies Division, Medical Research Council Laboratory of Molecular Biology, Cambridge, UK. ²Department of Infectious Diseases, Molecular Virology, Heidelberg University, Heidelberg, Germany. ³Department of Infectious Diseases, Virology, Heidelberg University, Heidelberg, Germany. ⁴Visual Aids Department, Medical Research Council Laboratory of Molecular Biology, Cambridge, UK. ⁵German Center for Infection Research, Heidelberg Partner Site, Heidelberg, Germany. ⁶Division of Virus-Associated Carcinogenesis, German Cancer Research Center (DKFZ), Heidelberg, Germany. ⁷These authors contributed equally: Zunlong Ke, Joaquin Oton, Kun Qu. ✉e-mail: jbriggs@mrc-lmb.cam.ac.uk

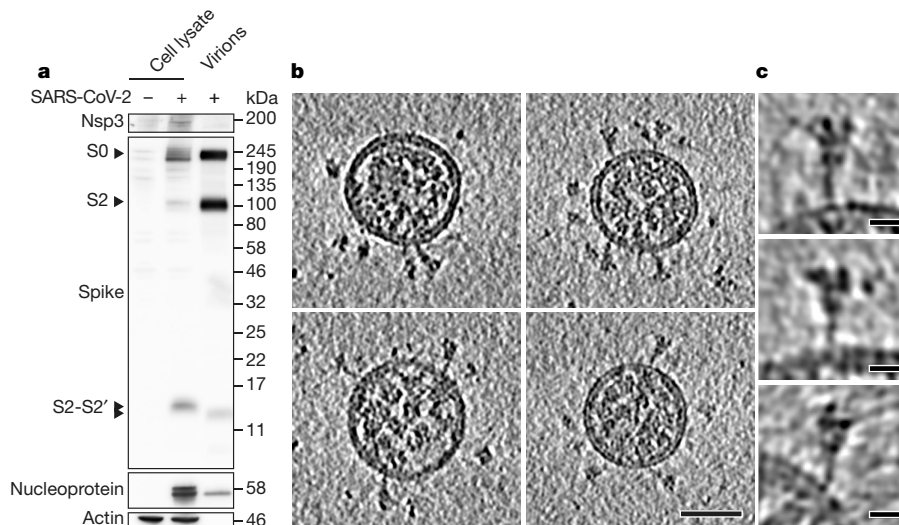


Fig. 1 | Characterization of virus production and images of SARS-CoV-2 virions. **a**, Western blot analysis of SARS-CoV-2 non-structural protein 3 (nsp3), S and N in lysates of Vero E6 cells and in virus preparations, representative of three experiments. In released virions, S is present in both cleaved and uncleaved forms. The positions of S0, S2 and the S2-S2' cleavage product are marked. **b**, Four representative tomographic slices of SARS-CoV-2 virions from

the supernatant of infected cells. Virions are approximately spherical, contain granular density corresponding to N-packaged genome, and have S trimers protruding at variable angles from their surfaces. Scale bar, 50 nm. **c**, Three S trimers from the dataset, shown as projections through the trimer to illustrate variable tilt towards the membrane. Scale bars, 10 nm.

was vitrified by plunge freezing and imaged by cryo-EM. Fixation may help to stabilize some protein conformations by crosslinking, but is not expected to give rise to any new conformations. As expected, given the concentration of virus in cellular supernatants (around 10^7 plaque-forming units per ml), small numbers of individual virions were found scattered around the grid—these were imaged by cryo-electron tomography (cryo-ET) (Fig. 1b).

Virions were approximately spherical, with a diameter to the outside of the lipid bilayer of 91 ± 11 nm ($n = 179$) (Extended Data Fig. 1a). They contained granular densities corresponding to N, and were studded with S trimers (Fig. 1b, c). These features are generally consistent with those of other coronaviruses imaged using cryo-EM^{1,16,17}. S trimers protruding from the viral surface displayed two distinct morphologies—a minority were extended thin structures reminiscent of the postfusion form, whereas the majority were wider structures reminiscent of the prefusion form. This observation is in contrast to a study showing cryo-EM images of purified SARS-CoV-2 virions inactivated with the nucleic acid modifier β -propiolactone, in which only thin protrusions were seen on the viral surface²⁵, but is consistent with in situ observations of virus assembly²¹.

We also collected tomograms of SARS-CoV-2 virions produced by infection of Calu-3 cells, a human lung carcinoma cell line that supports virus production with a similar titre to Vero E6 cells. The morphology of the virions and the appearance of the S trimers on the surface were consistent with those for virions produced from Vero E6 cells (Extended Data Fig. 2a–c). Western blot analysis showed that approximately 73% of S from Calu-3 supernatant was in the cleaved form (Extended Data Fig. 2d).

Individual virions contained 24 ± 9 S trimers (Extended Data Fig. 1b). This is fewer than previous estimates that assumed a uniform distribution of S²¹, because S was not uniformly distributed over the virus surface. A small sub-population of virions contained only few S trimers whereas larger virions contained higher numbers of S trimers (Extended Data Fig. 1b). We identified 4,104 wide-structure S trimers and 116 thin-structure S trimers from 179 virions and analysed them using subtomogram averaging. The averaged structures, at 7.7 and 22 Å resolution, respectively, correspond closely to published structures of purified S trimers in the prefusion and postfusion forms^{2,7,8} (Fig. 2a).

Overall, approximately 97% of S trimers were in the prefusion form and 3% were in the postfusion form. Prefusion and postfusion forms were evenly distributed among virions.

Prefusion S trimers on the virus surface may be predominantly in the closed conformation, with the open conformation induced or stabilized only with ACE2 binding; alternatively, both closed and open prefusion trimers may be present in the absence of ACE2. Open or closed conformations may induce different antibody responses when used as immunogens, and there are ongoing efforts to generate S protein constructs that are stabilized in specific conformations^{9,11,12}. To assess whether S trimers are present in open and/or closed conformations, we classified the RBD regions of individual monomers within trimers. We identified three classes of RBD, one with the RBD in the closed position, one with the RBD in the open position, and one in which the RBD was predominantly in the closed position, but showed some weakening of the density, suggesting the presence of more mobile conformations (Extended Data Fig. 3). On the basis of our assignment of individual monomers to these classes, we derived structures of fully closed trimers and of trimers in which one RBD was open, representing approximately 31% and 55% of 3,854 prefusion trimers, respectively (Fig. 2b, Extended Data Fig. 4). We also identified a small number of trimers (around 14% of 3,854 prefusion trimers) in which two RBDs were in the open conformation (Fig. 2b). These observations confirmed that the opening of the RBD observed in recombinant S trimers also takes place on the virus surface, and that artificial S protein constructs stabilized in the closed and open conformations both represent structures present in situ. The receptor-binding site is therefore stochastically exposed in situ and available to interact with ACE2 and with antibodies.

The trimers did not all protrude perpendicularly from the viral surface. They were tilted by up to 90° towards the membrane, although the frequency of observed tilt angles decreased above 50° (Extended Data Fig. 1c, d). We grouped trimers according to their orientation relative to the membrane, and averaged these groups independently. The averaged structures reveal that the membrane-proximal stalk region acts as a hinge with sufficient flexibility to allow tilting in all directions (Fig. 2c).

We generated models of individual virus particles, with S trimers located at the position, orientation and conformation that were

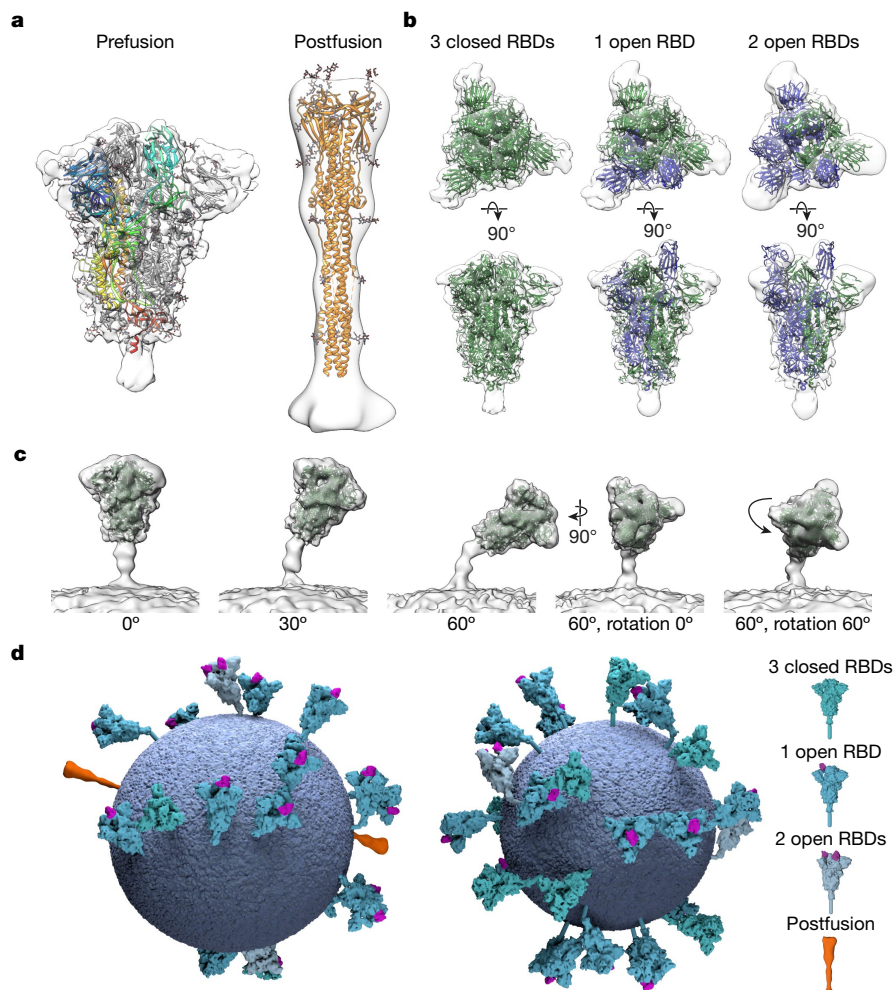


Fig. 2 | Structural analysis of SARS-CoV-2 S trimers on intact virions.

a, Structures of prefusion (left) and postfusion (right) trimers from intact virions, determined by subtomogram averaging. Structures are shown as transparent grey isosurfaces fitted with structures of the closed, prefusion trimer (Protein Data Bank (PDB) 6VXX) and the postfusion trimer (PDB 6XRA). One prefusion monomer is coloured blue (N terminus) to red (C terminus). The NTD is blue, the RBD is cyan. The NTD does not fully occupy the cryo-EM density because some loops are not resolved or built in the template structure (PDB 6VXX). **b**, Three conformations of the prefusion trimer observed on intact virions: all RBDs in the closed position (left, fitted with PDB 6VXX); one RBD in the open position (centre, fitted with PDB 6VYB); two RBDs in the open position (right, fitted with PDB 6X2B, which lacks modelled glycans). The two-open

conformation has only been observed in vitro after inserting multiple stabilizing mutations. S monomers with closed RBDs are green, and those with open RBDs are blue. **c**, Averaging of subsets of trimers grouped according to their orientation relative to the membrane shows flexibility in the stalk region. Examples are shown for pools centred at 0°, 30° and 60° from the perpendicular, and for two rotations of the trimer relative to the tilt direction. **d**, Three-dimensional models of two individual SARS-CoV-2 virions with a membrane (blue) of the measured radius, and all spike proteins shown in the conformations, positions and orientations determined by subtomogram averaging. Different S conformations are distributed over the virion surface and can be tilted by up to approximately 90° relative to the membrane (Extended Data Fig. 1c, d).

determined by subtomogram averaging (Fig. 2d). S trimers appear to be distributed randomly on the viral surface, with no obvious clustering or relationship between location, orientation and conformation. There is approximately one trimer per 1,000 nm² of membrane surface, compared with approximately one per 100 nm² for influenza A virus²⁶. The sparse distribution of S, together with the predominantly closed state, suggest that receptor binding may be less dependent on avidity effects than in the case of pandemic influenza viruses²⁷. This is consistent with the higher affinity between S and ACE2 (in the nM range^{2,7}) than between haemagglutinin and sialic acid (mM range²⁷).

The low concentration of particles in supernatant makes high-resolution structure determination difficult. We therefore concentrated the virus by pelleting through a sucrose cushion. Concentrated virions deviated from the spherical morphology (Extended Data Fig. 5), but the overall features were preserved. We performed cryo-ET and subtomogram averaging on the particles and observed predominantly

prefusion S trimers, with occasional postfusion S trimers. Upon classification of the prefusion S trimers, we were able to identify the RBD only in the closed position; weak RBD density was observed in monomers (Extended Data Fig. 3c).

Virions in the supernatant from infected cells exhibited primarily prefusion S trimers in either closed or open prefusion conformations. Virions concentrated through a sucrose cushion also exhibited prefusion conformations, but we did not observe the open conformation. Previous studies have shown that virions inactivated with β-propiolactone rather than formaldehyde are primarily in a postfusion state²⁵. S trimers purified from membranes are found only in the closed prefusion and postfusion conformations⁸, whereas the open RBD in soluble S trimers has been found to exhibit a wide range of different conformations²⁸. These observations suggest that the open prefusion conformations of the spike protein that we observed before, but not after concentration, are fragile (despite the fixation applied here) and may be affected by the purification procedures.

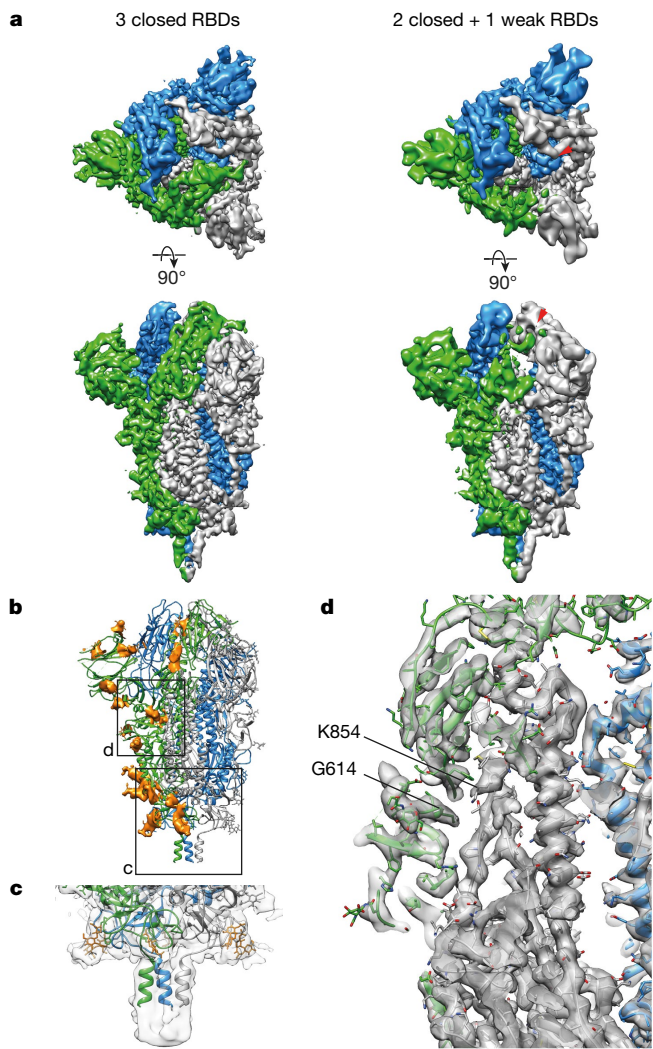


Fig. 3 | Structures of SARS-CoV-2 trimers on intact virions by single-particle reconstruction. **a**, Top and side views of trimers with three closed RBDs (left, 3.5 Å resolution) and one RBD with weaker density (right, 4.1 Å resolution). Individual monomers are coloured white, blue and green. Comparison of the left and right structures shows the weaker density for the RBD of the green monomer in the region indicated by the red arrowheads. **b**, Glycosylation profile of the S protein. Colour scheme as in **a**; glycans are shown in orange. Boxes indicate the regions shown in **c** and **d**. **c**, Enlarged view of the base of the trimer at lower isosurface threshold to highlight the glycan ring and the extended C-terminal density. **d**, Enlarged view of the region of the spike where the D614G variation abolishes a salt bridge to K854.

Our data indicate that inactivation and purification methods can alter the ratio of prefusion and postfusion forms, as well as the ratio of open and closed conformations. It has been suggested that substantial amounts of postfusion S on the virus surface may protect the virus by shielding the prefusion form, or may shift the host response towards non-neutralizing antibodies⁸. Our observation that intact virions harbour only a small fraction of postfusion spikes suggest that this is unlikely to be an important defence mechanism for the virus during infection, but it may be an important consideration for vaccination. Candidate vaccines based on inactivated virus particles are under development. These may present different S protein epitopes to the immune system depending on how they are prepared, and may therefore differ in their ability to induce a neutralizing response. For example, β -propiolactone is frequently used in vaccine production (such as for influenza virus subunit vaccines²⁹), but if postfusion S induces

non-neutralizing responses, β -propiolactone may not be optimal for inactivation during SARS-CoV-2 vaccine formulation.

We next imaged the concentrated virus in 2D using cryo-EM and performed single-particle analysis on prefusion S trimers that protruded from the sides of the virus particles, generating a consensus structure of the prefusion trimer at 3.4 Å resolution. Focused classification with partial signal subtraction on individual RBD monomers led to two classes (Extended Data Fig. 5). Consistent with the absence of open conformations in this sample in cryo-ET images, 81% of the monomers showed the RBD in the closed conformation and 19% showed weaker density for the RBD, which remained predominantly in the closed position. We refined the structures of S trimers in which all three RBDs are in the closed conformation (53% of the data), and those in which at least one RBD has weak density (47% of the data), to resolutions of 3.5 Å and 4.1 Å, respectively (Fig. 3a, Extended Data Fig. 6). The two structures are highly similar, differing only in the density levels for one RBD. We used the structure with three closed RBDs to build and refine an atomic model of the S protein trimer in situ on the viral surface.

The positions of glycans on the surface of S are well resolved in our structure, with density at 17 of the 22 predicted N-glycosylation sites (Fig. 3b). The other five glycosylation sites are in disordered NTD loops or in the stalk region and are not resolved at high resolution. At the base of the trimer, a clear ring of glycans forms a collar above the stalk region. The density for the stalk region is extended by two helical turns compared with published structures of soluble ectodomain, and further at lower resolution before fading owing to stalk flexibility (Fig. 3c). SARS-CoV-2 trimers are sparsely distributed and can be highly tilted towards the membrane. This implies that epitopes at the base of the head domain and in the stalk region would be accessible to antibodies where they are not protected by the extensive glycan shell.

We compared the in situ structure of the S trimer with structures previously obtained using exogenously expressed purified protein. A recent study of full-length trimeric S solubilized in detergent micelles⁸ identified two features that are not seen in most structures of soluble S ectodomain trimers: well-defined density for residues 14–26 of S, and a folded loop between residues 833 and 853. This loop is folded in the structure of the ‘locked’ conformation of the ectodomain⁹, and may become folded in the low-pH conditions in the endosome³⁰. We observed only weak density for residues 14–26, and no folded structure for the 833–853 region. The SARS-CoV-2 strain that we have imaged contains the widely circulating D614G substitution³¹, which abolishes a salt bridge to K854 (Fig. 3d) and may reduce folding of the 833–854 loop^{9,30}. We did not observe additional density that would correspond to bound lipids, as described recently¹⁰, or other bound co-factors. These may be present sub-stoichiometrically or in rare conformations, but are not a general feature of the S trimer in situ. Overall, our structure is very similar to that of the soluble trimeric ectodomain in the closed prefusion form stabilized by a double proline mutation^{2,7} (Extended Data Fig. 7). This validates the ongoing use of recombinant, purified S trimers for research, diagnostics and vaccination—they indeed represent the in situ structure of S. In this study, we have determined the structure of S trimers on the virion surface to 3.4 Å resolution using cryo-EM (Fig. 3), supporting the further use of this technique to study antibody binding to S in the context of the viral surface. Such studies could provide insights into how neutralizing antibodies block virus infection, particularly for antibodies against membrane-proximal regions of S, and thus can inform the design of immunogens for vaccination.

Online content

Any methods, additional references, Nature Research reporting summaries, source data, extended data, supplementary information, acknowledgements, peer review information; details of author contributions and competing interests; and statements of data and code availability are available at <https://doi.org/10.1038/s41586-020-2665-2>.

1. Neuman, B. W. & Buchmeier, M. J. Supramolecular architecture of the coronavirus particle. *Adv. Virus Res.* **96**, 1–27 (2016).
2. Walls, A. C. et al. Structure, function, and antigenicity of the SARS-CoV-2 spike glycoprotein. *Cell* **181**, 281–292 (2020).
3. Hoffmann, M. et al. SARS-CoV-2 cell entry depends on ACE2 and TMPRSS2 and is blocked by a clinically proven protease inhibitor. *Cell* **181**, 271–280 (2020).
4. Shang, J. et al. Structural basis of receptor recognition by SARS-CoV-2. *Nature* **581**, 221–224 (2020).
5. Wang, Q. et al. Structural and functional basis of SARS-CoV-2 entry by using human ACE2. *Cell* **181**, 894–904 (2020).
6. Watanabe, Y., Allen, J. D., Wrapp, D., McLellan, J. S. & Crispin, M. Site-specific glycan analysis of the SARS-CoV-2 spike. *Science* **369**, 330–333 (2020).
7. Wrapp, D. et al. Cryo-EM structure of the 2019-nCoV spike in the prefusion conformation. *Science* **367**, 1260–1263 (2020).
8. Cai, Y. et al. Distinct conformational states of SARS-CoV-2 spike protein. *Science* **369**, 1586–1592 (2020).
9. Xiong, X. et al. A thermostable, closed SARS-CoV-2 spike protein trimer. *Nat. Struct. Mol. Biol.* **27**, 934–941 (2020).
10. Toelzer, C. et al. Free fatty acid binding pocket in the locked structure of SARS-CoV-2 spike protein. *Science* eabd3255 (2020).
11. Henderson, R. et al. Controlling the SARS-CoV-2 spike glycoprotein conformation. *Nat. Struct. Mol. Biol.* **27**, 925–933 (2020).
12. McCallum, M., Walls, A. C., Bowen, J. E., Corti, D. & Veesler, D. Structure-guided covalent stabilization of coronavirus spike glycoprotein trimers in the closed conformation. *Nat. Struct. Mol. Biol.* **27**, 942–949 (2020).
13. Zhu, N. et al. A novel coronavirus from patients with pneumonia in China, 2019. *N. Engl. J. Med.* **382**, 727–733 (2020).
14. Zhou, P. et al. A pneumonia outbreak associated with a new coronavirus of probable bat origin. *Nature* **579**, 270–273 (2020).
15. Masters, P. S. & Perlman, S. in *Fields Virology* 6th edn (eds Knipe, D. M. & Howley, P. M.) 826–858 (Elsevier, 2013).
16. Neuman, B. W. et al. Supramolecular architecture of severe acute respiratory syndrome coronavirus revealed by electron cryomicroscopy. *J. Virol.* **80**, 7918–7928 (2006).
17. Bárcena, M. et al. Cryo-electron tomography of mouse hepatitis virus: insights into the structure of the coronavirus. *Proc. Natl Acad. Sci. USA* **106**, 582–587 (2009).
18. Walls, A. C. et al. Tectonic conformational changes of a coronavirus spike glycoprotein promote membrane fusion. *Proc. Natl Acad. Sci. USA* **114**, 11157–11162 (2017).
19. Yuan, Y. et al. Cryo-EM structures of MERS-CoV and SARS-CoV spike glycoproteins reveal the dynamic receptor binding domains. *Nat. Commun.* **8**, 15092 (2017).
20. Fehr, A. R. & Perlman, S. Coronaviruses: an overview of their replication and pathogenesis. *Methods Mol. Biol.* **1282**, 1–23 (2015).
21. Klein, S. et al. SARS-CoV-2 structure and replication characterized by in situ cryo-electron tomography. Preprint at <https://doi.org/10.1101/2020.06.23.167064> (2020).
22. Snijder, E. J. et al. A unifying structural and functional model of the coronavirus replication organelle: tracking down RNA synthesis. *PLoS Biol.* **18**, e3000715 (2020).
23. Hoffmann, M., Hofmann-Winkler, H. & Pöhlmann, S. in *Activation of Viruses by Host Proteases* (eds Böttcher-Friebertshäuser, E. et al.) 71–98 (2018).
24. Rothe, C. et al. Transmission of 2019-nCoV infection from an asymptomatic contact in Germany. *N. Engl. J. Med.* **382**, 970–971 (2020).
25. Liu, C. et al. Viral architecture of SARS-CoV-2 with post-fusion spike revealed by cryo-EM. Preprint at <https://doi.org/10.1101/2020.03.02.972927> (2020).
26. Chlanda, P. et al. The hemifusion structure induced by influenza virus haemagglutinin is determined by physical properties of the target membranes. *Nat. Microbiol.* **1**, 16050 (2016).
27. Xiong, X. et al. Receptor binding by a ferret-transmissible H5 avian influenza virus. *Nature* **497**, 392–396 (2013).
28. Gui, M. et al. Cryo-electron microscopy structures of the SARS-CoV spike glycoprotein reveal a prerequisite conformational state for receptor binding. *Cell Res.* **27**, 119–129 (2017).
29. Bonnafous, P. et al. Treatment of influenza virus with beta-propiolactone alters viral membrane fusion. *Biochim. Biophys. Acta* **1838**, 355–363 (2014).
30. Zhou, T. et al. A pH-dependent switch mediates conformational masking of SARS-CoV-2 spike. Preprint at <https://doi.org/10.1101/2020.07.04.187989> (2020).
31. Korber, B. et al. Tracking changes in SARS-CoV-2 spike: evidence that D614G increases infectivity of the COVID-19 virus. *Cell* **182**, 812–827 (2020).

Publisher's note Springer Nature remains neutral with regard to jurisdictional claims in published maps and institutional affiliations.

© The Author(s), under exclusive licence to Springer Nature Limited 2020

Methods

No statistical methods were used to predetermine sample size. For Cryo-ET, division of dataset into two random halves was done based on virus number. For Cryo-EM, division of datasets into two random halves was done based on the standard approach in RELION 3. Other experiments did not involve randomization. The investigators were not blinded to allocation during experiments and outcome assessment.

Cells and virus

Vero E6 cells were obtained from ATCC and were cultured in Dulbecco's modified Eagle medium (DMEM, Life Technologies) containing 10% fetal bovine serum, 100 U ml⁻¹ penicillin, 100 µg ml⁻¹ streptomycin and 1% non-essential amino acids (complete medium). The Germany/Bav-Pat1/2020 SARS-CoV-2 strain was isolated by C. Drosten (Charité, Berlin, distributed by the European Virology Archive (Ref-SKU: 026V-03883)) at passage (P)2. A stock of SARS-CoV-2 was obtained by passaging the virus once in Vero E6 cells (P3). To produce SARS-CoV-2 virions, Vero E6 cells grown on 75 cm² side-bottom tissue culture flasks were infected with SARS-CoV-2 (P3) at a multiplicity of infection (MOI) of 0.5. Culture medium from infected cells was collected at 48 h after infection, clarified by centrifugation at 1,000g for 10 min, cleared through a 0.45-µm nitrocellulose filter and fixed with 4% formaldehyde for 30 min at room temperature. Culture medium was supplemented with 10 mM HEPES (pH 7.2) before fixation. Virus-containing medium was subsequently split into aliquots and stored at -80 °C. Infectious supernatants containing SARS-CoV-2 virions were obtained from Calu-3 cells infected with P3 virus at an MOI of 5 for 48 h and processed as described above.

To obtain SARS-CoV-2 virions at high concentration, infection and collection of Vero E6 culture medium were performed as above, followed by concentration of fixation-inactivated virions from medium by ultracentrifugation through a 20% (wt/wt) sucrose cushion (120 min at 27,000 rpm in a Beckman SW32 rotor; Beckman Coulter Life Sciences). Pelleted particles were resuspended in PBS and stored in aliquots at -80 °C.

Western blot

Vero E6 or Calu-3 cells mock infected or infected for 48 h with SARS-CoV-2 (MOI = 5) were washed twice in PBS, scraped, pelleted at 700g for 5 min and lysed in PBS pH 7.4, containing 1% Triton X-100 and protease inhibitors (Merck) for 30 min at 4 °C. Samples were centrifuged at 4 °C for 30 min and supernatants were collected. Total protein concentration was calculated using the Bio-Rad Protein Assay kit (Bio-Rad). Purified viruses were prepared for western blot by centrifugation of 32 ml of virus containing supernatants on a 10% sucrose cushion in a Beckmann J25 centrifuge. Centrifugation was performed at 10,000g for 4 h at 4 °C. Supernatants were discarded and purified virus pellet were resuspended in 500 µl PBS. For western blotting, 10 µg of total cell lysates and 5 µl purified viruses were diluted in Laemmli buffer and loaded on a pre-cast Criterion XT 4-12% gradient gel (Bio-Rad). Gels were transferred to PVDF membrane using a wet-electroblotting chamber system (Bio-Rad) in Towbin buffer containing 10% methanol. Transfer was performed overnight at 4 °C. Membranes were washed in PBS and blocked with 10% milk in PBS containing 0.2% tween-20 (PBS-T) for 1 h. Membranes were incubated for 1 h at room temperature with primary antibodies specific for an epitope in the C-terminal region of S (Abcam, ab252690; diluted 1:1,000 in PBS-T), for N protein (Sino Biological, 40143-MM05; diluted 1:1,000 in PBS-T) or nsp3 (Abcam, ab181620; diluted 1:500 in PBS-T). Next, the membranes were washed 3 times in PBS-T, incubated with horseradish peroxidase-conjugated anti-mouse or anti-rabbit antibodies at 1:10,000 dilution for 1 h, washed again 3 times in PBS-T, incubated with western Lightning Plus-ECL reagent (Perkin Elmer) and imaged using an Intas ChemoCam Imager 3.2 (Intas). Densitometric analysis of western blot assays was performed using LabImage 1D L340 software v.4.1 (Intas). The blot shown is

representative of three independent experiments. Uncropped, unprocessed blots are presented in the Source Data.

PCR with reverse transcription and spike sequencing

Total RNA was isolated from infected Vero E6 cells 48 h after infection with Germany/BavPat1/2020 SARS-CoV-2 (P2). Spike cDNA was produced from the total RNA using Superscript III (ThermoFisher) with specific reverse transcription primer (CAATTGTGAAGATTCTC ATA). The cDNA was amplified by PCR using specific primers (Fwd, ATGTTTGT TTTTCTGT TTTTATT; rev, TTATGTGTAATGTAATTGA) and the resulting amplicon was sent for Sanger sequencing. Sequences were compared to the Germany/BatPat1/2020 SARS-CoV-2 reference sequence (Ref-SKU: 026V-03883) and found to be identical. Specific sequencing primers: Fwd1, ATGTTTGT TTTTCTGT TTTTATT; Fwd2, GGTGGACAGCTGGTGCT; Fwd3, CCAACCATACAGAGTAGTAGTA; Rev1, GTAGCAGCAAGATTAGCAGAA; and Rev2, TTATGTGTAATGT AATTGA.

Cryo-ET sample preparation

Fixed virus samples from the supernatant of infected cells without any concentration step (unconc) or concentrated by pelleting through a sucrose cushion (conc) were prepared, imaged, and processed in parallel. The virus suspension was mixed with 10-nm colloidal gold (in PBS solution) in 10:1 ratio. Then, 3 µl of the solution was added to a glow-discharged copper grid (C-Flat 2/2, Protochips). Grids were plunge frozen into liquid ethane by back-side blotting using a LeicaGP cryo plunger (Leica) and stored in liquid nitrogen until imaging.

Cryo-ET data collection

Cryo-ET data collection was performed essentially as described previously³². Cryo-grids were loaded into an FEI Titan Krios transmission electron microscope operated at 300 kV and images were recorded on a Gatan K2 Summit direct detection camera in counting mode with a 20 eV energy slit in zero-loss mode. Tomographic tilt series between -60° and +60° were collected using SerialEM 3.8.0 software³³ in a dose-symmetric scheme³⁴ with a 3° angular increment. A total dose of 120 e⁻ Å⁻² per tilt series was distributed evenly among 41 tilt images. The nominal magnification was 81,000×, giving a pixel size of 1.532 Å on the specimen. The defocus range was between -2 µm and -6 µm and 10 frames were saved for each tilt angle. All data acquisition parameters are listed in Extended Data Table 1.

Frames were motion-corrected in IMOD 4.10.30³⁵ and images were dose-filtered using the alignframes function in IMOD. Exposure filtering was implemented according to the cumulative dose per tilt as described elsewhere³⁶. The contrast transfer function (CTF) was measured using non-dose-filtered images using the ctfplotter package within IMOD³⁷. Tilt series stacks were sorted using IMOD newstack function and fiducial-alignment of all tilt series was performed in IMOD/etomo. Tomograms with less than three trackable gold fiducials were discarded. Motion-corrected and dose-filtered tilt stacks were CTF-corrected by CTF multiplication and tomograms were reconstructed by weighted back-projection in novaCTF³⁸. Tomograms were low-pass filtered to 50 Å for better visualization in EMAN2.2³⁹ and tomographic slices were visualized with IMOD.

Extraction of S trimers from tomograms

The initial steps of subtomogram alignment and averaging were implemented using MATLAB (MathWorks) scripts, which were derived from the TOM⁴⁰ and AV3⁴¹ packages as described previously³². The missing wedge was modelled as the summed amplitude spectrum of background subtomograms for each tomogram, and was applied during alignment and averaging.

To generate an initial template model of the spike protein from the viral surface, 68 spikes were manually picked from four virions of tomograms that were down-scaled by 4× binning of the voxels.

Article

The 68 spikes' initial Euler angles (2 out of 3) were determined on the basis of the vector between two points, one on the head of the spike and one on the membrane where the spike anchors, respectively. The 68 spikes were iteratively aligned to one another for four iterations, applying three-fold symmetry to generate a low-resolution template that resembled a prefusion conformation of the spike. This template was used as an alignment reference for all virions (below). All postfusion spikes were manually identified and picked, and initial Euler angles were assigned in the same manner.

The centre of each virion was then marked manually using the Volume Tracer function in UCSF Chimera (v.1.13.1)⁴² and the radius of the virion was determined centred at the membrane using the Pick Particle Chimera Plugin⁴³. An oversampled spherical grid of points was generated on the virion surface with -9 nm spacing, and subtomograms were extracted for all grid points with a box size of 96 pixels (approximately 60 nm) centred at a radius 14 nm above these grid positions (approximately the radius of the expected centre of the spike). Initial Euler angles were assigned to each subtomogram based on the orientation of the normal vectors relative to the sphere surface.

Subtomograms were aligned against the low-resolution template (from the above average of 68 spikes). During this alignment, subtomogram positions converged onto clusters at the true spike positions. One subtomogram position was kept for each cluster, excluding particles within a distance of -60 Å (10 pixels at 4× binning) and removing particles with cross-correlation coefficients below 0.11. Subtomograms that had tilted by more than 90° relative to their perpendicular positions were excluded. Visual inspection of the tomograms using the Place Object Chimera Plugin⁴³ confirmed that subtomograms selected in this manner corresponded to S trimers on the viral surface (see below). Subtomograms were divided into two halves on the basis of virion number. From this point on the two halves were processed independently.

Subtomogram averaging

Subsequent processing was performed in RELION⁴⁴. For this purpose, subtomograms were reconstructed from the original tilt series images after motion correction using `relion_reconstruct`. Using dedicated Python scripts, the S trimer positions in the 3D tomograms from the procedure outlined above were converted into 2D positions and defocus values in the corresponding tilt series images, as well as Euler angles in the RELION convention. Individual sub-tomograms were reconstructed at a 2× downsampled pixel size of 3.064 Å, by 3D insertion of Fourier slices of the cropped regions of the tilt series images, each multiplied by their corresponding CTF, which included the dose filter. Similarly, 3D-CTF volumes were generated by 3D insertion of the corresponding CTF² slices. Subtomograms were reconstructed in a box size of 128 voxels for prefusion trimers and a box size of 192 voxels for averages of tilted prefusion trimers and for postfusion trimers.

To deal with the CTF pre-multiplied sub-tomograms, as well as the multiplicity of each 3D voxel in the tilt series, a modified version of RELION was used for subtomogram refinement and classification (details to be described elsewhere). Standard 3D auto-refinement was performed with C3 symmetry and a soft-edged mask around the trimers, using a 30 Å lowpass-filtered map as an initial reference. Using 3,854 of the 4,104 subtomograms (excluding those that had tilted by more than 90° relative to the perpendicular position (Extended Data Fig. 1c)), a 7.7 Å consensus map was calculated for the prefusion trimers; 116 postfusion trimers led to a 22 Å map.

Angular density (Extended Data Fig. 1c) was illustrated by dividing the number of spikes per histogram bin by the sine of the tilt angle. From this histogram, the noise level in the distribution due to incorrectly aligned spikes was estimated assuming they are uniformly distributed (red dashed line in Extended Data Fig. 1c), and based on averaging over the range 140–180°. Such angles must be incorrectly alignments because they orient the spike towards the inside of the virus.

Based on the subtomograms that contributed to the consensus map we estimated that there are 23 ± 9 prefusion S trimers per virion. For a subset of 28 virions, we visually compared the trimers identified by subtomogram averaging with the tomograms to identify false positives or false negatives, finding that the number of S trimers identified by subtomogram averaging is an underestimate of the number of observed S trimers by 0.9 trimers per virion. On this basis we estimate there are 24 ± 9 prefusion S trimers per virion.

Next, we performed symmetry expansion⁴⁵, followed by focused classification without alignment and with partial signal subtraction, while keeping the orientations from the consensus refinement fixed. The mask used for focused classification was generated manually and enclosed the RBD of one monomer (Extended Data Fig. 3a), including the closest NTD of the neighbouring monomer. Classification of the primary dataset (unconcl) led to three different RBD states: closed (45% of the monomers); open (28%) and with weak density (27%) (Extended Data Fig. 3a). Classification of a second, smaller dataset of virus particles in supernatant (unconcl2), comprising 1,224 trimers yielded 39% closed RBD, 22% open RBD and 39% weak RBD, in general agreement with the unconcl results (Extended Data Fig. 3b). Classification of a dataset of virus particles after concentration through a sucrose cushion (conc), comprising 3,788 trimers, yielded 67% of the monomers corresponding to closed RBDs and 33% to RBDs with weak density. For this dataset, no RBDs in the open conformation were identified (Extended Data Fig. 3c).

The classification of the RBDs as closed, open or with weaker density was used to divide the unconcl dataset into three subsets: 31% (1,175 trimers) have no open RBDs; 55% (2,121 trimers) have one RBD in the open state; and 14% (525 trimers) have two open RBDs. The remaining 33 trimers have three RBDs in the open state and not further processed. In the class with weaker density, the RBD appears to be predominantly in the closed state and was treated as closed for this assignment. For each of the three subsets, reconstruction of the two independently refined half sets was performed using the orientations from the consensus refinement that gave the 7.7 Å consensus map described above. Subsequent standard post-processing procedures for resolution estimation, map sharpening and local-resolution filtering in RELION led to three final maps. The subset with no open RBDs gave a reconstruction with C3 symmetry in which all three RBDs were closed at 8.6 Å resolution. The other two subsets yielded structures with C1 symmetry and either one or two open RBDs, with resolutions of 8.6 Å and 9.9 Å, respectively (Extended Data Figs. 3, 4). Note, that while fixation is not expected to give rise to any new conformations, we cannot rule out that it differentially stabilizes different conformations, and the position of the equilibrium between open and closed conformations in unfixed samples may differ from those estimated from fixed samples.

Averages of tilted prefusion trimers were generated by grouping according to the tilt and rotation of the subtomogram away from the normal vector to the membrane. Subtomograms were included in a group for averaging if they were within 15° of the displayed tilt (0°, 30° and 60°) and rotation (0°, 60°). The pools illustrated in Fig. 2c contain 14.5, 14.1, 12.0 and 10.0% of the subtomograms.

Cryo-EM sample preparation and data collection

Virus solution concentrated through a 20% (wt/wt) sucrose cushion was plunge-frozen on C-Flat 2/2 3C grids (Protochips) following the same procedure as for cryo-ET, but without adding gold fiducials. Grids were imaged on a Thermo Fisher Scientific Titan Krios transmission electron microscope that was operated at 300 kV, using a Gatan K3 direct electron detector and a Gatan BioQuantum energy filter with a 20 eV energy slit. Movies with 48 frames and an accumulated dose of $50 \text{ e}^- \text{ \AA}^{-2}$ were acquired in counting mode using SerialEM-3.8.0³³ at a nominal magnification of 81,000×, corresponding to a calibrated pixel size of 1.061 Å per pixel. Detailed data acquisition parameters are summarized in Extended Data Table 2.

Cryo-EM image processing

The scheduler functionality in RELION-3.1 was used for fully automated real-time processing during data collection^{9,46}. Movies were motion-corrected and dose-weighted using the RELION implementation of the MotionCor2 algorithm⁴⁷. Subsequently, non-dose-weighted sums were used to estimate the CTF in CTFFIND-4.1.13⁴⁸. S trimers that were extending from the sides of virus particles were picked manually (4,493 particles from the first 100 micrographs) and then used as a training set for optimisation of the convolutional neural network in the automated particle picking software Topaz⁴⁹. Extracted particles were subjected to 3D classification using a previously determined structure of the S trimer⁹, low-pass-filtered to 30 Å, as initial 3D reference. The selected 286,407 particles that contributed to 3D classes corresponding to S trimers were submitted to Bayesian polishing to correct for per-particle beam-induced motions and a second round of 3D classification to select the 55,159 particles that contributed to the best class. This final consensus set of particles was subjected to CTF refinement of per-particle defocus, per-micrograph astigmatism and beam tilt, followed by a second round of Bayesian polishing. 3D auto-refinements were performed with the selected particles after each round of 3D classification, CTF refinement or Bayesian polishing. The consensus structure had a resolution of 3.4 Å.

Subsequently, symmetry expansion⁴⁵ was performed, followed by focused 3D classification with partial signal subtraction⁵⁰. Using a mask on a single RBD to focus classification into six classes while keeping the orientations of the last consensus refinement fixed resulted in the identification of two RBD states: closed or with weak density. S trimers with all three RBDs in the closed state were refined separately from S trimers with one RBD with weak density, resulting in two final maps with resolutions. Standard RELION post-processing was used for resolution estimation, map sharpening and local-resolution filtering. The C3 symmetric map with three closed RBDs had an estimated overall resolution of 3.5 Å; the C1 map with one weaker RBD extended to 4.1 Å resolution (Extended Data Fig. 6b).

Model building and refinement

The SARS-CoV-2 S trimer structure⁹ (PDB 6ZP0) was used as an initial model for building into the model with three closed RBDs (Extended Data Fig. 6a, middle). Residues were adjusted manually in Coot 0.9⁵¹. Steric clash and sidechain rotamer conformations were improved using the Namdinator web server⁵². After further iterations of manual adjustment, the structure was refined in PHENIX-1.18.2⁵³. The geometry and statistics are given in Extended Data Table 2. The unmasked model-to-map FSC was calculated in PHENIX for the refined model against the full reconstruction.

3D model of spikes on authentic virions

To visualize the spike protein on the authentic SARS-CoV-2 virions, the coordinates, orientations and conformational classes determined by subtomogram averaging were converted into a format compatible with Maxon Cinema 4D (v.S22.116), and imported together with the 3D models of the different conformational states determined by subtomogram averaging. To generate representative virion images in Fig. 2d we removed the three false positives from one virion and positioned the three false negatives on each virion that had been identified by visual inspection of the data (see above). The HR2 region was modelled as a cylinder. Images of individual virions from the dataset were rendered into Adobe Photoshop to generate images for presentation.

Reporting summary

Further information on research design is available in the Nature Research Reporting Summary linked to this paper.

Data availability

Published structures for comparison or initial model building were obtained from the PDB with accession codes 6VXX², 6VYB², 6X2B¹¹, 6XRA⁸ and 6ZP0⁹. The cryo-EM and cryo-ET structures determined here and representative tomograms are deposited in the Electron Microscopy Data Bank (EMDB) under accession codes EMD-11493 (prefusion consensus structure), EMD-11494 (three closed RBDs from subtomogram averaging), EMD-11495 (one open RBD), EMD-11496 (two open RBDs), EMD-11497 (three closed RBDs from cryo-EM), and EMD-11498 (two open RBDs and one weak RBD). The associated molecular models are deposited in the PDB under accession code 6ZWV (three closed RBDs from cryo-EM). The raw micrographs are deposited in the Electron Microscopy Public Image Archive under accession codes EMPIAR-10492 (cryo-EM) and EMPIAR-10493 (cryo-ET).

- Wan, W. et al. Structure and assembly of the Ebola virus nucleocapsid. *Nature* **551**, 394–397 (2017).
- Mastronarde, D. N. Automated electron microscope tomography using robust prediction of specimen movements. *J. Struct. Biol.* **152**, 36–51 (2005).
- Hagen, W. J. H., Wan, W. & Briggs, J. A. G. Implementation of a cryo-electron tomography tilt-scheme optimized for high resolution subtomogram averaging. *J. Struct. Biol.* **197**, 191–198 (2017).
- Kremer, J. R., Mastronarde, D. N. & McIntosh, J. R. Computer visualization of three-dimensional image data using IMOD. *J. Struct. Biol.* **116**, 71–76 (1996).
- Grant, T. & Grigorieff, N. Measuring the optimal exposure for single particle cryo-EM using a 2.6 Å reconstruction of rotavirus VP6. *eLife* **4**, e06980 (2015).
- Xiong, Q., Morpew, M. K., Schwartz, C. L., Hoenger, A. H. & Mastronarde, D. N. CTF determination and correction for low dose tomographic tilt series. *J. Struct. Biol.* **168**, 378–387 (2009).
- Turoňová, B., Schur, F. K. M., Wan, W. & Briggs, J. A. G. Efficient 3D-CTF correction for cryo-electron tomography using NovaCTF improves subtomogram averaging resolution to 3.4 Å. *J. Struct. Biol.* **199**, 187–195 (2017).
- Galaz-Montoya, J. G., Flanagan, J., Schmid, M. F. & Ludtke, S. J. Single particle tomography in EMAN2. *J. Struct. Biol.* **190**, 279–290 (2015).
- Nickell, S. et al. TOM software toolbox: acquisition and analysis for electron tomography. *J. Struct. Biol.* **149**, 227–234 (2005).
- Förster, F., Medalia, O., Zauberman, N., Baumeister, W. & Fass, D. Retrovirus envelope protein complex structure in situ studied by cryo-electron tomography. *Proc. Natl Acad. Sci. USA* **102**, 4729–4734 (2005).
- Petersen, E. F. et al. UCSF Chimera—a visualization system for exploratory research and analysis. *J. Comput. Chem.* **25**, 1605–1612 (2004).
- Qu, K. et al. Structure and architecture of immature and mature murine leukemia virus capsids. *Proc. Natl Acad. Sci. USA* **115**, E11751–E11760 (2018).
- Bharat, T. A. M., Russo, C. J., Löwe, J., Passmore, L. A. & Scheres, S. H. W. Advances in single-particle electron cryomicroscopy structure determination applied to sub-tomogram averaging. *Structure* **23**, 1743–1753 (2015).
- Scheres, S. H. W. Processing of structurally heterogeneous cryo-EM data in RELION. *Methods Enzymol.* **579**, 125–157 (2016).
- Zivanov, J. et al. New tools for automated high-resolution cryo-EM structure determination in RELION-3. *eLife* **7**, e42166 (2018).
- Zheng, S. Q. et al. MotionCor2: anisotropic correction of beam-induced motion for improved cryo-electron microscopy. *Nat. Methods* **14**, 331–332 (2017).
- Rohou, A. & Grigorieff, N. CTFFIND4: fast and accurate defocus estimation from electron micrographs. *J. Struct. Biol.* **192**, 216–221 (2015).
- Bepler, T. et al. Positive-unlabeled convolutional neural networks for particle picking in cryo-electron micrographs. *Nat. Methods* **16**, 1153–1160 (2019).
- Bai, X. C., Rajendra, E., Yang, G., Shi, Y. & Scheres, S. H. W. Sampling the conformational space of the catalytic subunit of human γ -secretase. *eLife* **4**, e11182 (2015).
- Emsley, P. & Cowtan, K. Coot: model-building tools for molecular graphics. *Acta Crystallogr. D* **60**, 2126–2132 (2004).
- Kidmose, R. T. et al. Namdinator—automatic molecular dynamics flexible fitting of structural models into cryo-EM and crystallography experimental maps. *IUCr* **6**, 526–531 (2019).
- Afonine, P. V. et al. Real-space refinement in PHENIX for cryo-EM and crystallography. *Acta Crystallogr. D* **74**, 531–544 (2018).

Acknowledgements We thank the staff of the MRC-LMB for generous support during the COVID-19 pandemic lockdown; all of the staff of the MRC-LMB EM Facility, in particular A. Yeates, G. Sharov and G. Cannone, for supporting the EM experiments; J. Grimmett and T. Darling for supporting scientific computing; C. Drosten and EVAg for provision of the SARS-CoV-2 strain used here; and M. Frey for the Calu-3 cell line. We acknowledge microscopy support from the Infectious Diseases Imaging Platform (IDIP) at the Center for Integrative Infectious Disease Research Heidelberg. This study was supported by funding from the European Research Council (ERC) under the European Union's Horizon 2020 research and innovation programme (ERC-CoG-648432 MEMBRANEFUSION to J.A.G.B.), the Medical Research Council as part of UK Research and Innovation (MC_UP_A025_1013 to S.H.W.S.; MC_UP_1201/16 to J.A.G.B.), the Deutsche Forschungsgemeinschaft (240245660-SFB 1129 project 5 to H.-G.K. and project 11 to R.B.) and the Japan Society for the Promotion of Science (overseas research fellowship to T.N.).

Article

Author contributions Z.K. and J.A.G.B. conceived the study. Z.K., J.O., K.Q., M.C., V.Z., H.-G.K., R.B. and J.A.G.B. designed the study. M.C., V.Z., C.J.N. and B.C. prepared and characterized virus samples with supervision from H.-G.K. and R.B. Z.K. and K.Q. collected cryo-EM data. Z.K., J.O. and K.Q. processed cryo-EM data with assistance from T.N., J.Z., J.M.L. and J.P., supervised by S.H.W.S. and J.A.G.B. Z.K., J.O., K.Q., M.C. and L.M. made figures. Z.K., J.O., K.Q., M.C., X.X. and J.A.G.B. interpreted data. J.A.G.B. prepared the initial draft and managed the project. Z.K., J.O., K.Q., M.C. and J.A.G.B. wrote the manuscript with input from all authors. S.H.W.S., H.-G.K., R.B. and J.A.G.B. obtained funding.

Competing interests The authors declare no competing interests.

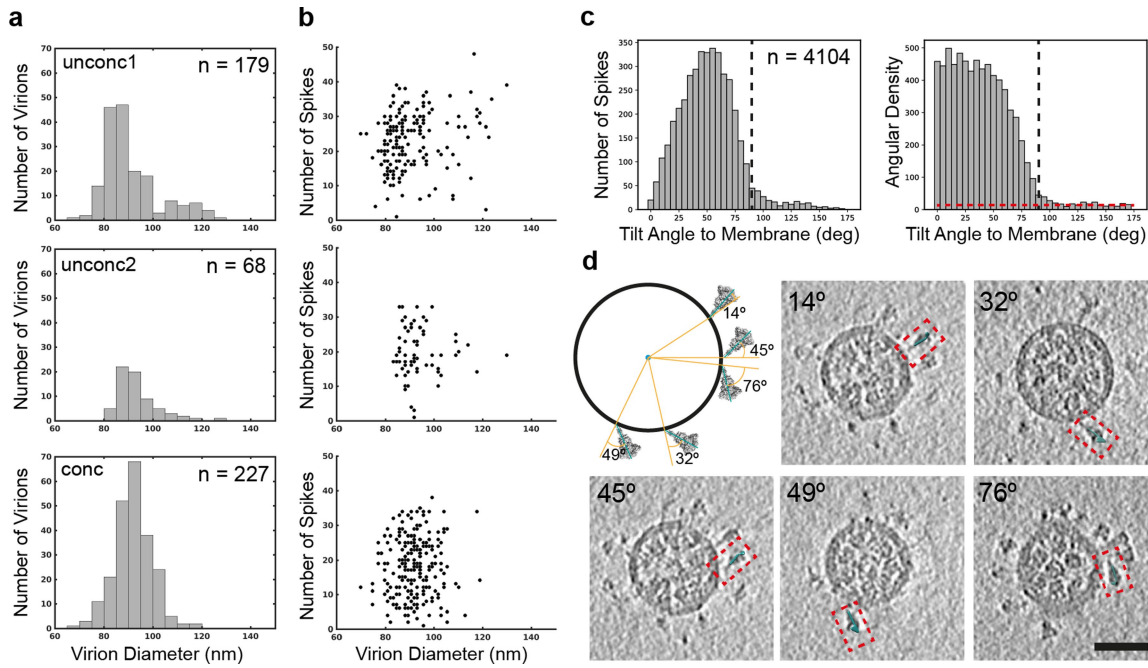
Additional information

Supplementary information is available for this paper at <https://doi.org/10.1038/s41586-020-2665-2>.

Correspondence and requests for materials should be addressed to J.A.G.B.

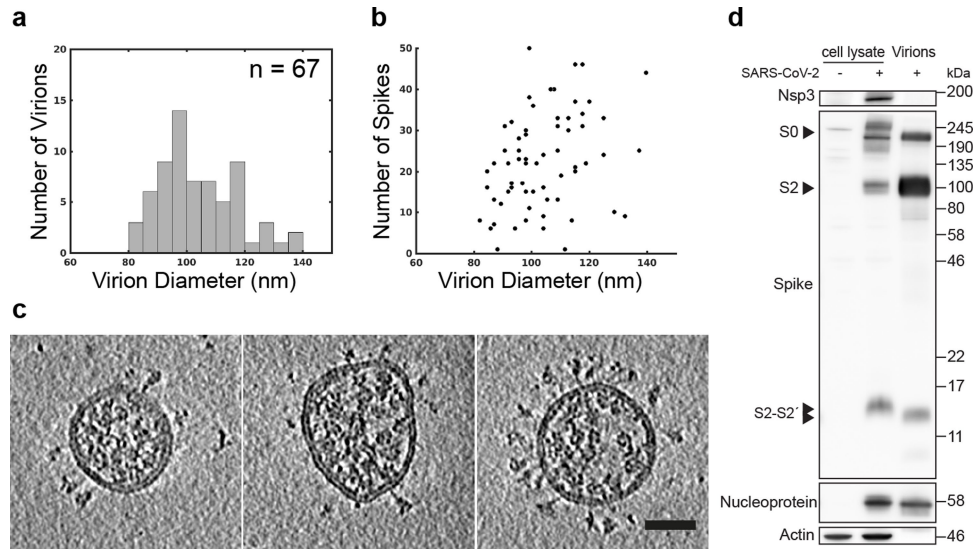
Peer review information *Nature* thanks Jason McLellan and the other, anonymous, reviewer(s) for their contribution to the peer review of this work. Peer reviewer reports are available.

Reprints and permissions information is available at <http://www.nature.com/reprints>.



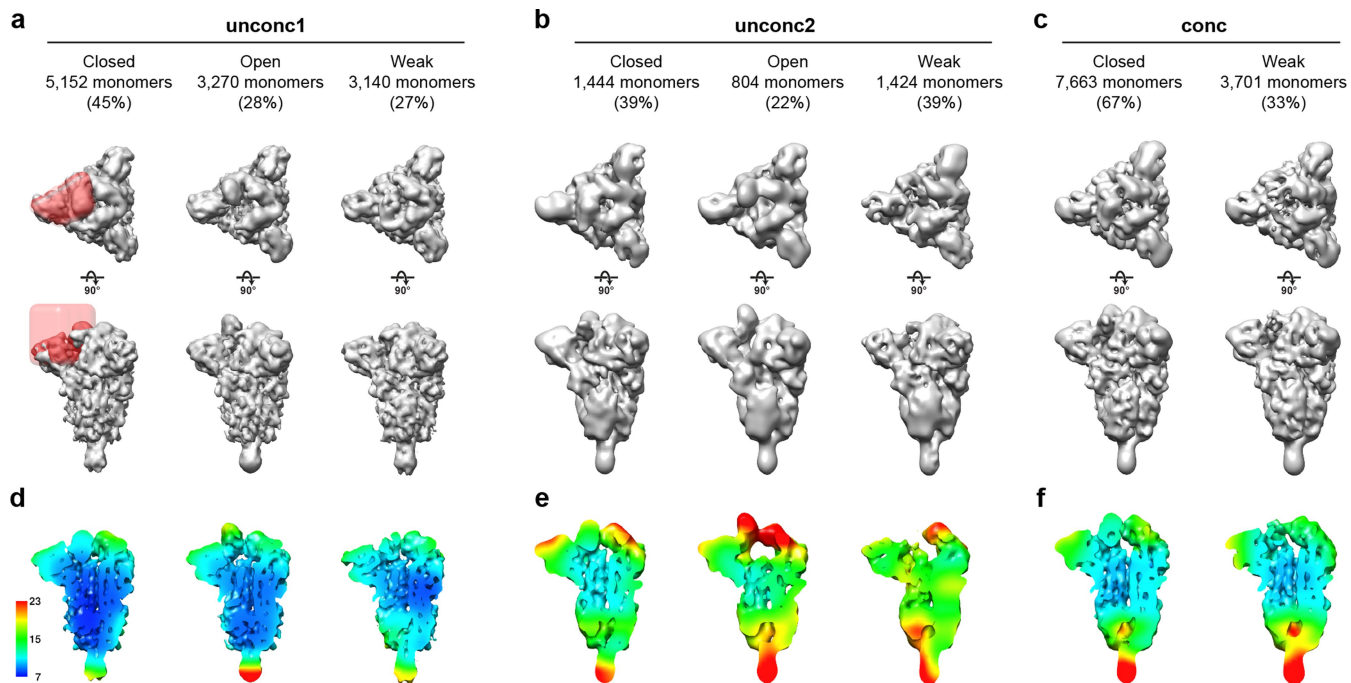
Extended Data Fig. 1 | Characterization of SARS-CoV-2 virion morphology. **a**, Histogram of virion diameters for unconcentrated extracellular virions in the supernatant of two independent preparations (top and middle), and for extracellular virions after concentration through a sucrose cushion (bottom). After concentration the virions become less spherical. Mean and standard deviation for diameters are 91 ± 11 nm ($n = 179$), 94 ± 9 nm ($n = 68$) and 92 ± 8 nm ($n = 227$) for the three preparations. **b**, Scatter plot of number of spikes identified per virion during subtomogram averaging against virion diameter for the same virions shown in **a**. Visual inspection indicates that almost all spikes were identified for virions in the supernatant, but that not all spikes are identified in the concentrated preparation leading to an underestimate of the number of spikes. **c**, Histogram of spike tilt angle towards the membrane for the

larger supernatant virus dataset (unconc1). The vertical black dashed line indicates 90° . 97% of particles have tilts below 90° ; particles with tilts above 90° were not included in image analysis. The angular density (right) is calculated by dividing the number of spikes by the sine of the determined angle. If spikes were unconstrained in tilt, this distribution would be uniform. The angular density decreases from ~ 500 at 0° to ~ 100 at 180° , indicating that higher tilts are disfavoured. The horizontal red dashed line indicates the angular distribution of noise (spikes which have failed to align), estimated based on the angular density between 140° and 180° . **d**, Schematic diagram and examples of individual tilted spikes on virions. The schematic indicates the angle that was measured. Five examples of individual tilted spikes are marked on tomographic slices through an intact virion, with their associated angle. Scale bar 50 nm.



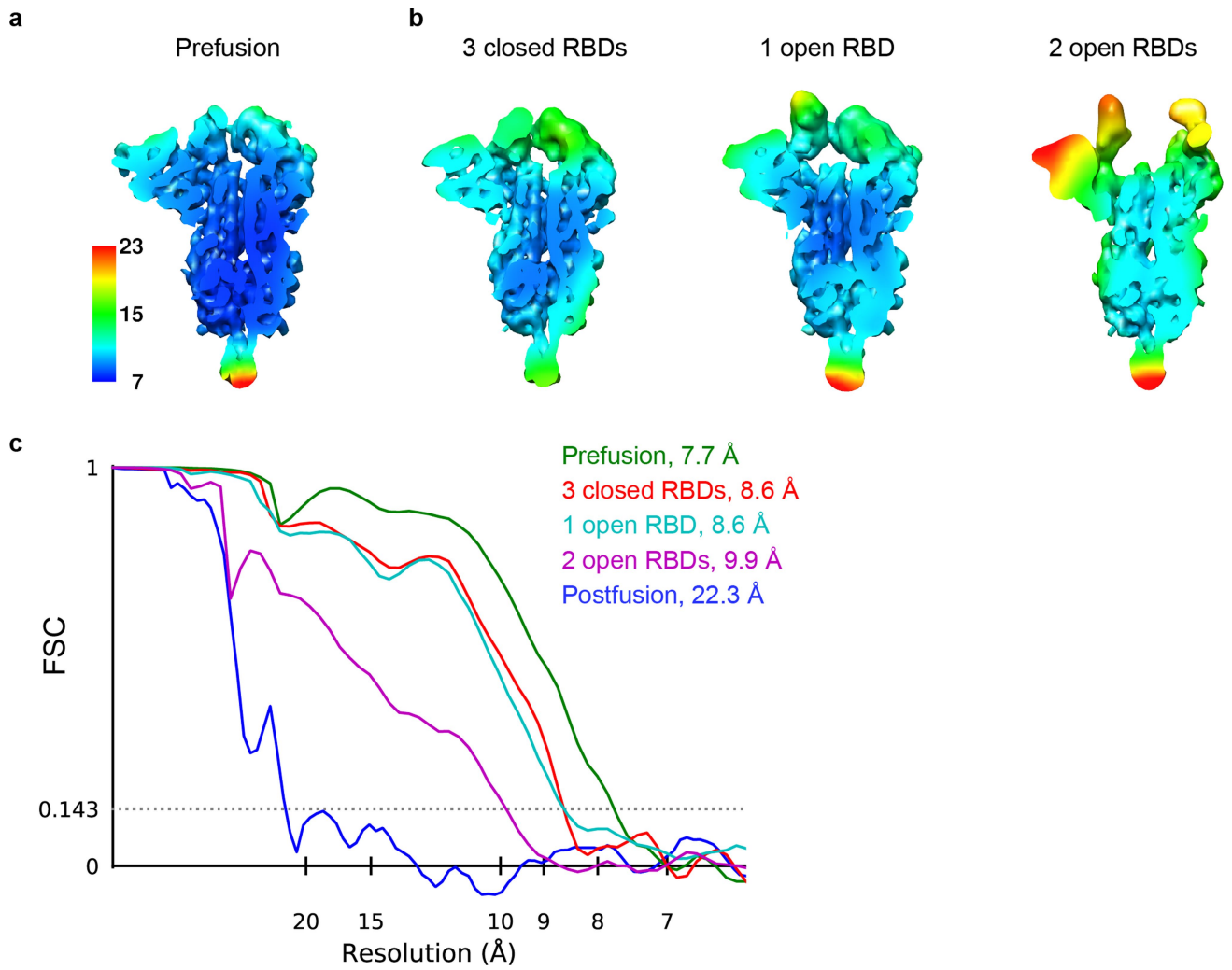
Extended Data Fig. 2 | Morphology of SARS-CoV-2 virions released from infected Calu-3 cells. As in Extended Data Fig. 1. **a**, Histogram of virion diameters. Mean and standard deviation for diameters are 104 ± 13 nm ($n = 67$). **b**, Scatter plot of number of spikes identified per virion during subtomogram averaging against virion diameter for the same virions shown in **a**. **c**, Central

slices through three representative viruses from 67 imaged in one experiment. Virions from Calu-3 cells had a slightly broader diameter distribution than those from Vero E6 cells. Scale bar 50 nm. **d**, Western blot analysis of SARS-CoV-2 nsp3, S and N in cell lysates and in virus preparations. In released virions, S is present in both cleaved (S2, 73%) and uncleaved forms (S0, 27%).



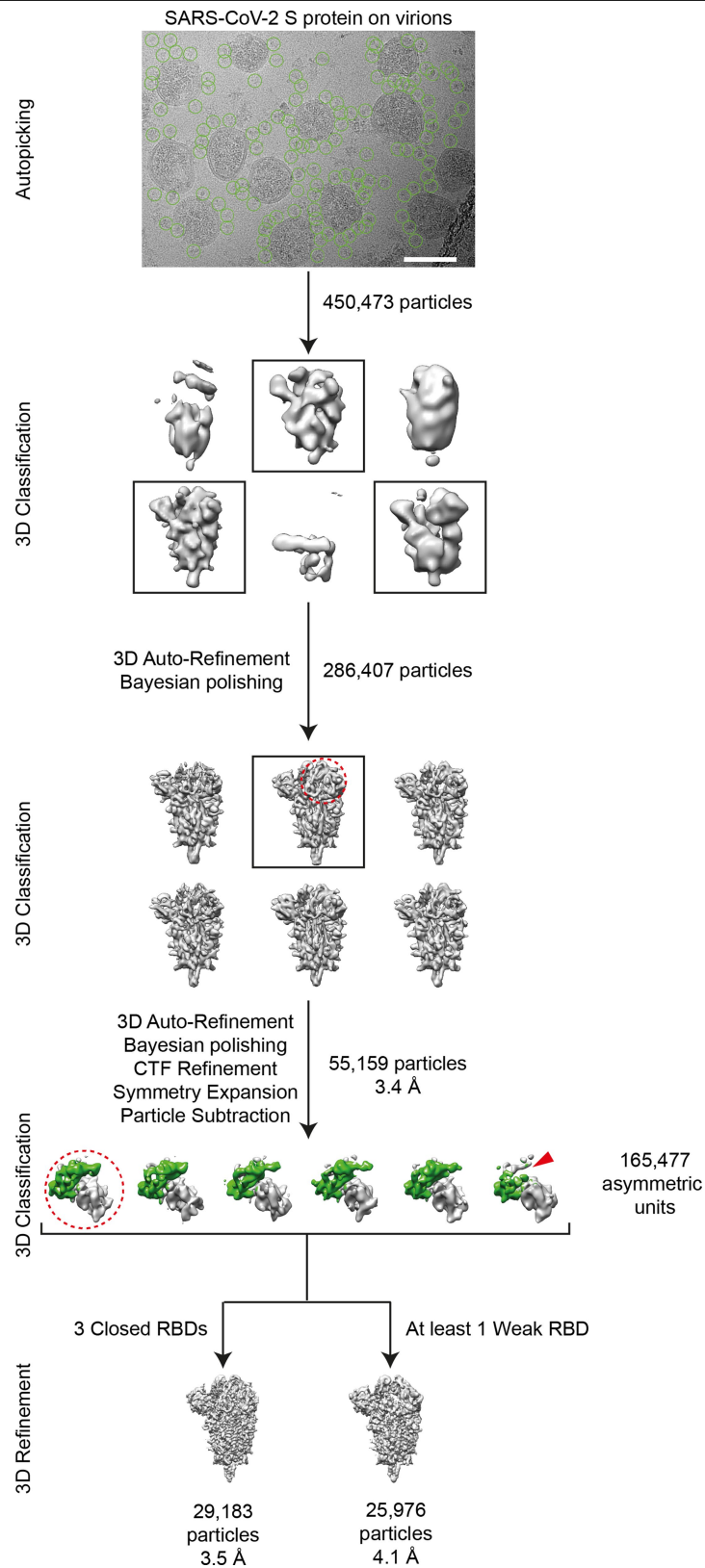
Extended Data Fig. 3 | Classification of SARS-CoV-2 spike RBDs. **a**, Class averages obtained after focused classification on the RBD of the left monomer after symmetry expansion of the unconc1 dataset. Top views and side views are shown for closed, open and weak classes. The region subjected to classification is indicated by a transparent red mask surface in the left hand

panel. **b**, Equivalent analysis for a smaller, independent dataset (unconc2). **c**, Equivalent analysis for a dataset obtained after concentrating virus through a sucrose cushion (conc). Only closed and weak classes were obtained. **d-f**, Cut-open local resolution maps for structures shown in **a-c**.



Extended Data Fig. 4 | Resolution assessment of subtomogram averaging structures. **a**, Local resolution map for the consensus structure obtained for the prefusion S trimers. **b**, Local resolution maps for the prefusion S trimer in

three different conformations. **c**, Global resolution assessment by Fourier shell correlation (FSC) at the 0.143 criterion for the four structures shown in **a** and **b**, as well as the postfusion S trimer.

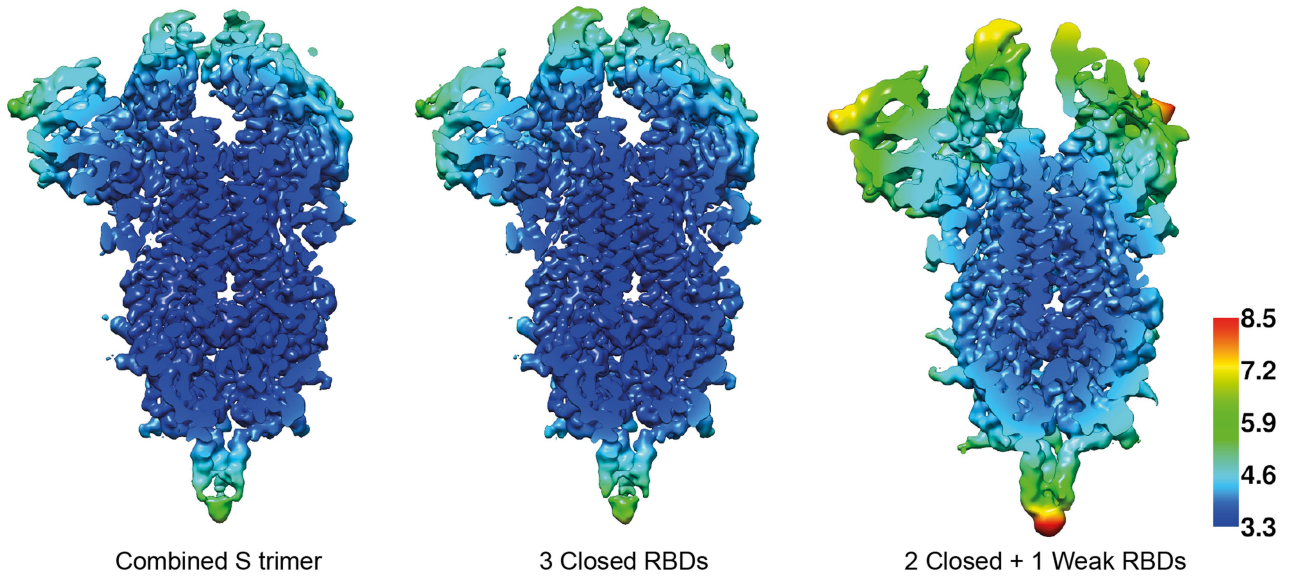


Extended Data Fig. 5 | Single particle cryo-EM image processing workflow.

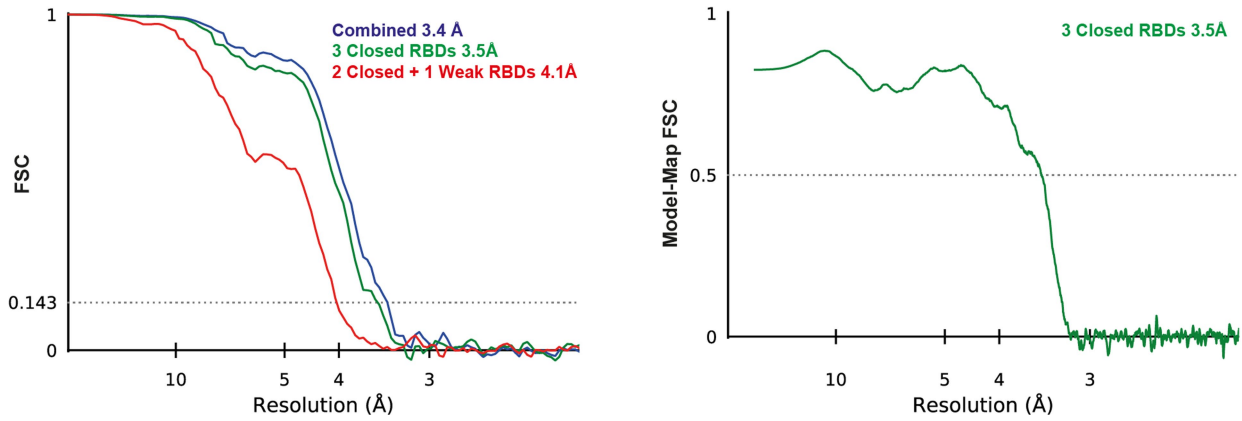
Automatically picked particles (green circles) were subjected to 3D classification. Scale bar 100 nm. Selected 3D classes are indicated by black boxes. RBDs from individual asymmetric units from the S trimer (red dashed circles) were locally classified to sort different conformations of RBD. The

asymmetric unit subjected to local classification is shown in a top view, the RBD of the green monomer is weak in the right-hand class (red arrowhead). S trimers with all three RBDs in the closed state were further refined with C3 symmetry. S trimers where one RBD had weak density were refined with C1 symmetry. For further details see materials and methods.

a



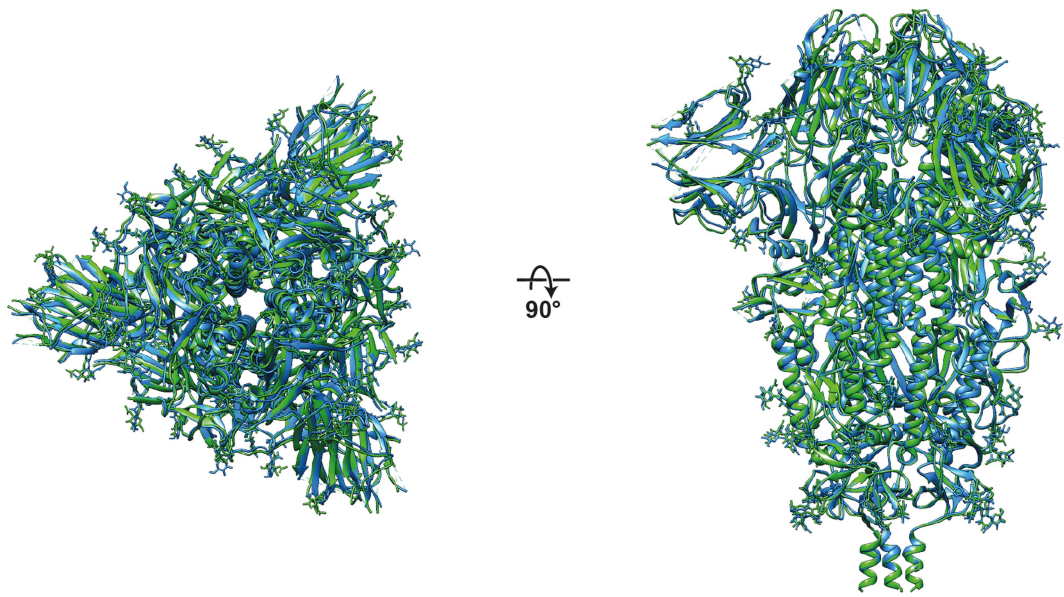
b



Extended Data Fig. 6 | Single particle Cryo-EM structure validation.

a, Cut-open cryo-EM maps obtained using all prefusion S trimers, S trimers with 3 closed RBDs or S trimers with 2 closed and 1 weak RBDs, coloured according

to the local resolution. **b**, FSC curves for the three structures in **a**, and for the atomic model against the map.



Extended Data Fig. 7 | Structural comparison of in situ structure with recombinant soluble structure. Structural superposition of S trimer modelled into the structure of the trimer with three closed RBDs

(green, this study) with the published structure of recombinant, soluble closed trimer (blue, PDB 6VXX). Top and side views are shown. The structures are very similar.

Article

Extended Data Table 1 | Cryo-ET data acquisition and image processing

Sample	VeroE6 unconc 1	VeroE6 unconc 2	VeroE6 conc	Calu-3 unconc
Data Collection				
Microscope	FEI Titan Krios	FEI Titan Krios	FEI Titan Krios	FEI Titan Krios
Voltage (keV)	300	300	300	300
Energy-filter (eV)	20	20	20	20
Detector	Gatan K2 Summit	Gatan K2 Summit	Gatan K2 Summit	Gatan K2 Summit
Recording Mode	Counting	Counting	Counting	Counting
Pixel size (Å)	1.532	1.532	1.532	1.532
Defocus range (µm)	-2 to -6	-2 to -6	-2 to -6	-2 to -6
Acquisition scheme	-60/60°, 3°	-60/60°, 3°	-60/60°, 3°	-60/60°, 3°
Total Dose (electrons/Å ²)	~120	~120	~120	~120
Frame number	10	10	10	10
Tomograms	156	65	30	57
Image processing				
Virus particles	179	68	227	NA
Subtomograms	4,104	1,335	4,136	NA
Symmetry	C3	C3	C3	NA
Resolution at 0.143 FSC (Å)	7.7	9.9	9.1	NA
EMDB ID	EMD-11493	NA	NA	
Spike trimer conformation classification				
Trimer Classification	3 closed RBDs	1 open RBD	2 open RBDs	
Trimer particles	1,175	2,121	525	
Symmetry	C3	C1	C1	
Resolution at 0.143 FSC (Å)	8.6	8.6	9.9	
EMDB ID	EMD-11494	EMD-11495	EMD-11496	

Extended Data Table 2 | Cryo-EM data collection, refinement and validation statistics

	3 Closed RBDs (EMD-11497, PDB 6ZWW)	2 Closed + 1 Weak RBDs (EMD-11498)
Data collection and processing		
Magnification	81,000	81,000
Voltage (kV)	300	300
Electron exposure (e ⁻ /Å ²)	50	50
Defocus range (µm)	1.0-3.0	1.0-3.0
Pixel size (Å)	1.061	1.061
Movies (no.)	7,982	7,982
Symmetry imposed	<i>C3</i>	<i>C1</i>
Initial particle images (no.)	450,473	450,473
Final particle images (no.)	29,183	25,976
Map resolution (Å)	3.5	4.1
FSC threshold	0.143	0.143
Map resolution range (Å)	3.35-27.16	3.67-45.27
Refinement		
Initial model used	PDB 6ZP0	
Model resolution (Å)	3.5	
FSC threshold	0.5	
Map sharpening <i>B</i> factor (Å ²)	-50	
Model composition		
Non-hydrogen atoms	24036	
Protein residues	2955	
Ligands	63	
<i>B</i> factors (Å ²)		
Protein	130.57	
Ligand	142.74	
R.m.s. deviations		
Bond lengths (Å)	0.009	
Bond angles (°)	1.346	
Validation		
MolProbity score	1.62	
Clashscore	2.97	
Poor rotamers (%)	1.74	
Ramachandran plot		
Favored (%)	94.97	
Allowed (%)	5.03	
Disallowed (%)	0.00	

Reporting Summary

Nature Research wishes to improve the reproducibility of the work that we publish. This form provides structure for consistency and transparency in reporting. For further information on Nature Research policies, see our [Editorial Policies](#) and the [Editorial Policy Checklist](#).

Statistics

For all statistical analyses, confirm that the following items are present in the figure legend, table legend, main text, or Methods section.

- | n/a | Confirmed |
|-------------------------------------|--|
| <input type="checkbox"/> | <input checked="" type="checkbox"/> The exact sample size (n) for each experimental group/condition, given as a discrete number and unit of measurement |
| <input type="checkbox"/> | <input checked="" type="checkbox"/> A statement on whether measurements were taken from distinct samples or whether the same sample was measured repeatedly |
| <input checked="" type="checkbox"/> | <input type="checkbox"/> The statistical test(s) used AND whether they are one- or two-sided
<i>Only common tests should be described solely by name; describe more complex techniques in the Methods section.</i> |
| <input checked="" type="checkbox"/> | <input type="checkbox"/> A description of all covariates tested |
| <input checked="" type="checkbox"/> | <input type="checkbox"/> A description of any assumptions or corrections, such as tests of normality and adjustment for multiple comparisons |
| <input type="checkbox"/> | <input checked="" type="checkbox"/> A full description of the statistical parameters including central tendency (e.g. means) or other basic estimates (e.g. regression coefficient) AND variation (e.g. standard deviation) or associated estimates of uncertainty (e.g. confidence intervals) |
| <input checked="" type="checkbox"/> | <input type="checkbox"/> For null hypothesis testing, the test statistic (e.g. F , t , r) with confidence intervals, effect sizes, degrees of freedom and P value noted
<i>Give P values as exact values whenever suitable.</i> |
| <input checked="" type="checkbox"/> | <input type="checkbox"/> For Bayesian analysis, information on the choice of priors and Markov chain Monte Carlo settings |
| <input checked="" type="checkbox"/> | <input type="checkbox"/> For hierarchical and complex designs, identification of the appropriate level for tests and full reporting of outcomes |
| <input checked="" type="checkbox"/> | <input type="checkbox"/> Estimates of effect sizes (e.g. Cohen's d , Pearson's r), indicating how they were calculated |

Our web collection on [statistics for biologists](#) contains articles on many of the points above.

Software and code

Policy information about [availability of computer code](#)

Data collection	SerialEM 3.8.0 for operation of electron microscope (available and referenced in the Methods section)
Data analysis	<p>CryoET data processing (all commercial or available and referenced in methods): CTFFIND4; IMOD 4.10; NovaCTF 1.0.0, EMAN2.2; Matlab R2016b; TOM (no version number); AV3 (no version number); Python 3.7; RELION 3.1.</p> <p>CryoEM data processing (all available and referenced in methods): CTFFIND4.1.13; RELION 3.1.</p> <p>Modelling/structure refinement/visualization (all available and referenced in methods): Coot 0.9; Namdinator (no version numbering); PHENIX 1.18.2; Chimera 1.13.1; Maxon Cinema 4D version S22.116</p> <p>Western blot quantification: LabImage 1D L340 software version 4.1 (Intas, Göttingen)</p>

For manuscripts utilizing custom algorithms or software that are central to the research but not yet described in published literature, software must be made available to editors and reviewers. We strongly encourage code deposition in a community repository (e.g. GitHub). See the Nature Research [guidelines for submitting code & software](#) for further information.

Data

Policy information about [availability of data](#)

All manuscripts must include a [data availability statement](#). This statement should provide the following information, where applicable:

- Accession codes, unique identifiers, or web links for publicly available datasets
- A list of figures that have associated raw data
- A description of any restrictions on data availability

Published structures for comparison or initial model building were obtained from the protein data bank (PDB) with accession codes 6VXX, 6VYB, 6X2B, 6XRA and 6ZP0. The cryo-EM and cryo-ET structures determined here, and representative tomograms are deposited in the Electron Microscopy Data Bank (EMDB) under accession codes EMD-11493 (prefusion consensus structure), EMD-11494 (3 closed RBDs from subtomogram averaging), EMD-11495 (1 open RBD), EMD-11496 (2 open RBDs), EMD-11497 (3 closed RBDs from cryo-EM), and EMD-11498 (2 open and 1 weak RBDs). The associated molecular models are deposited in the PDB under accession codes 6ZWV (3 closed RBDs from cryo-EM).

Field-specific reporting

Please select the one below that is the best fit for your research. If you are not sure, read the appropriate sections before making your selection.

- Life sciences Behavioural & social sciences Ecological, evolutionary & environmental sciences

For a reference copy of the document with all sections, see [nature.com/documents/nr-reporting-summary-flat.pdf](https://www.nature.com/documents/nr-reporting-summary-flat.pdf)

Life sciences study design

All studies must disclose on these points even when the disclosure is negative.

Sample size	Sample sizes were determined by available electron microscopy time and the number of virus particles on electron microscopy grids. The sample size is sufficient to obtain a structure at the reported resolution, as assessed by Fourier shell correlation.
Data exclusions	For all cryo-ET experiments, tomograms which could not be used due to objects (contamination, ice, grid bars etc) obscuring the virus particle were discarded.
Replication	For cryoET and cryoEM, structures were determined from independent half datasets, which were compared to assess the resolution of the reconstruction, as described in the methods section. Two independent preparations of virus in supernatant were analysed as described in the methods section. Western blots are representative of three independent experiments.
Randomization	For CryoET, division of dataset into two random halves was done based on virus number. For CryoEM, division of datasets into two random halves was done based on standard approach in RELION 3. Other experiments did not involve randomization.
Blinding	Blinding was not applicable to this study because this type of study does not use group allocation.

Reporting for specific materials, systems and methods

We require information from authors about some types of materials, experimental systems and methods used in many studies. Here, indicate whether each material, system or method listed is relevant to your study. If you are not sure if a list item applies to your research, read the appropriate section before selecting a response.

Materials & experimental systems

- | n/a | Involved in the study |
|-------------------------------------|---|
| <input type="checkbox"/> | <input checked="" type="checkbox"/> Antibodies |
| <input type="checkbox"/> | <input checked="" type="checkbox"/> Eukaryotic cell lines |
| <input checked="" type="checkbox"/> | <input type="checkbox"/> Palaeontology and archaeology |
| <input checked="" type="checkbox"/> | <input type="checkbox"/> Animals and other organisms |
| <input checked="" type="checkbox"/> | <input type="checkbox"/> Human research participants |
| <input checked="" type="checkbox"/> | <input type="checkbox"/> Clinical data |
| <input checked="" type="checkbox"/> | <input type="checkbox"/> Dual use research of concern |

Methods

- | n/a | Involved in the study |
|-------------------------------------|---|
| <input checked="" type="checkbox"/> | <input type="checkbox"/> ChIP-seq |
| <input checked="" type="checkbox"/> | <input type="checkbox"/> Flow cytometry |
| <input checked="" type="checkbox"/> | <input type="checkbox"/> MRI-based neuroimaging |

Antibodies

Antibodies used

Anti-mouse HRP Sigma A4416
Anti-rabbit HRP Sigma A6154
Beta actin Sigma A5441
Spike Abcam Ab252690

Nsp3 abcam ab181620
Nucleocapsid Sino Biological 40143-MM05

Validation

Commercial antibodies validated as per manufacturers website:
Beta actin Sigma A5441 Immunoblot on chicken fibroblast cell extracts
Spike Abcam Ab252690 Validated by ELISA on free peptide from SARS-CoV-1
Nsp3 abcam ab181620 Validated by western blot on SARS-CoV-1 infected cells
Nucleocapsid Sino Biological 40143-MM05 Validated by western blot with corresponding viruses

Eukaryotic cell lines

Policy information about [cell lines](#)

Cell line source(s)

VeroE6 cells were obtained from ATCC, Calu-3 cells were obtained from Manfred Frey, originally from ATCC.

Authentication

Cells were not further authenticated

Mycoplasma contamination

Cells have been tested and are free of mycoplasma.

Commonly misidentified lines (See [ICLAC](#) register)

none